

Signatures of topology in quantum quench dynamics and their interrelation

Lorenzo Pastori, Simone Barbarino, and Jan Carl Budich

*Institute of Theoretical Physics, Technische Universität Dresden,
and Würzburg-Dresden Cluster of Excellence ct.qmat, 01062 Dresden, Germany*

Motivated by recent experimental progress in the study of quantum systems far from equilibrium, we investigate the relation between several dynamical signatures of topology in the coherent time-evolution after a quantum quench. Specifically, we study the conditions for the appearance of entanglement spectrum crossings, dynamical quantum phase transitions, and dynamical Chern numbers. For non-interacting models, we show that in general there is no direct relation between these three quantities. Instead, we relate the presence of level crossings in the entanglement spectrum to localized boundary modes that may not be of topological origin in the conventional sense. Finally, we investigate how interactions influence the presence of entanglement spectrum crossings and dynamical quantum phase transitions, by means of time-dependent density matrix renormalization group simulations.

I. INTRODUCTION

Founded on the general notion of topological phases of matter [1–3], physical phenomena reflecting topological properties by now have been predicted and observed in a broad variety of systems. While in conventional solid-state settings topological states are typically realized at low temperatures, recent advances in quantum simulators, e.g. implemented with ultra-cold atomic gases [4–6], provide new opportunities for detecting dynamical signatures of topology in quantum matter far from equilibrium [7–10]. There, an enormous tunability enables the implementation of a wide range of topological models [11–18] (see [7–9] for recent reviews), and the high degree of isolation allows for the realization of coherent quantum many-body dynamics over relatively long timescales.

A common protocol to investigate the interplay between topology and dynamics is to perform a quantum quench, where the system is initialized in a topologically trivial state that can be prepared at low entropy, before some parameters in its Hamiltonian are changed to a topological regime. In this scenario, numerous non-equilibrium signatures witnessing the change of topology have been identified [19–44], including dynamical quantum phase transitions [35–40] (DQPTs), entanglement spectrum crossings [41–43] (ESCs), and a dynamical Chern number [44] (DCN). These concepts characterize the post-quench time-evolution from quite different physical perspectives. For quench protocols within the same Altland-Zirnbauer (AZ) symmetry class [45–47], it is known that DQPTs appear as a consequence of crossing a quantum critical point between a trivial and a topological phase [36, 37, 39, 48]. By contrast, ESCs are a quantum information signature generalizing the presence of protected boundary modes in the entanglement spectrum [49–52], thus representing an instantaneous property of the time-evolved state [34]. Instead, the DCN is a topological invariant defined over a dimensionally extended space-time domain [44].

In this work, we present a comprehensive study of the relations between DQPTs, ESCs, and DCN as

fingerprints of non-equilibrium topology in quantum quench dynamics, focusing on the fully microscopic study of one-dimensional systems. We consider quantum quenches that are not necessarily restricted to a certain AZ symmetry class, and explicitly construct quench protocols exhibiting most of the possible combinations regarding the presence and absence of DQPT, ESC, and DCN (see Table I), where the absence of the few unobserved combinations is motivated with a simple geometric picture. In this sense, our results imply that there is no one-to-one correspondence between any of pair of those three signatures.

When constraining the quench protocol to a given AZ class, all three signatures individually still constitute a hallmark of some non-trivial topological properties in quench dynamics, albeit an earlier suggested direct correspondence between ESC and DCN [43] has been partly refuted [33, 34, 53]. Here, going beyond the notion of symmetry-preserving quenches, we show how these features generally are neither related to topological properties of the pre- and post-quench Hamiltonians, nor to an emergent topology of the time-evolved state. Instead, we observe how these signatures can be dynamically generated even by quenches between topologically trivial Hamiltonians, and how the ESCs can occur as a consequence of accidental boundary modes having no topological origin. Finally, by means of time-dependent density matrix renormalization group [54, 55] (DMRG) simulations, we first investigate the robustness of ESCs and DQPTs against interactions, and finally show how such signatures can appear after a quench of the interaction strength in a correlated version of the Su-Schrieffer-Heeger model [56].

This paper is structured as follows. In Sec. II, we briefly review how ESCs, DQPTs and DCN can be calculated for two-banded systems out of equilibrium. In Sec. III and IV A we present our results in the non-interacting and in the interacting regime, respectively. We finally conclude in Sec. V.

II. MODEL AND INDICATORS OF TOPOLOGY

In this section, we introduce the general framework and notations to be used throughout this article. We consider a one-dimensional chain of spinless fermions with a number L of unit cells, each one consisting of two orbitals, or sublattice sites, labeled with A and B . We denote the fermionic operators annihilating a spinless fermion on sublattices A and B with \hat{a}_j and \hat{b}_j , respectively, where $j = 1, \dots, L$. In the following, we will focus on the case where the system is initially prepared in the ground state $|\Psi\rangle$ of a pre-quench Hamiltonian $\hat{H} = \sum_{i,j} \hat{\Pi}_i^\dagger h_{i,j} \hat{\Pi}_j$, with $\hat{\Pi}_j^\dagger = (\hat{a}_j^\dagger \ \hat{b}_j^\dagger)$. At time $t = t_0$ the Hamiltonian of the system is suddenly switched to $\hat{H}' = \sum_{i,j} \hat{\Pi}_i^\dagger h'_{i,j} \hat{\Pi}_j$ such that, for $t > t_0$, the state of the system will be $|\Psi(t)\rangle = \hat{U}(t)|\Psi\rangle$, with $\hat{U}(t) = e^{-i\hat{H}'(t-t_0)}$ being the unitary time-evolution operator. Without loss of generality we assume $t_0 = 0$ and observe that, at each time t after the quantum quench, the time-evolved state $|\Psi(t)\rangle$ is the ground state of a time-dependent Hamiltonian:

$$\hat{H}_P(t) = e^{-i\hat{H}'t} \hat{H} e^{+i\hat{H}'t}, \quad (1)$$

called *parent* Hamiltonian [43], which satisfies the equation of motion $i\partial_t \hat{H}_P(t) = [\hat{H}', \hat{H}_P(t)]$ with the initial condition $\hat{H}_P(0) = \hat{H}$. From this definition, it is clear that the spectrum of the parent Hamiltonian coincides with that of the pre-quench Hamiltonian. In the following we will focus on systems with periodic boundary conditions, and the momentum state description becomes a convenient basis for the explicit calculation of the parent Hamiltonian in the two-band models considered. We introduce the momentum space operators $\hat{a}_k = \sum_j e^{ikj} \hat{a}_j / \sqrt{L}$ and $\hat{b}_k = \sum_j e^{ikj} \hat{b}_j / \sqrt{L}$, with $k = 2\pi n/L$ and $n = -L/2, \dots, L/2 - 1$. In this basis the parent Hamiltonian reads as $\hat{H}_P(t) = \sum_k \hat{\Pi}_k^\dagger h_P(k, t) \hat{\Pi}_k$ where $\hat{\Pi}_k^\dagger = (\hat{a}_k^\dagger \ \hat{b}_k^\dagger)$, and $h_P(k, t) = \vec{d}_P(k, t) \cdot \vec{\sigma}$, with $\vec{\sigma}$ being the vector of the three Pauli matrices acting in the sublattice space and $\vec{d}_P(k, t)$ the Bloch vector characterizing $\hat{H}_P(t)$. The Bloch Hamiltonian $h_P(k, t)$ for a single momentum k satisfies $i\partial_t h_P(k, t) = [h'(k), h_P(k, t)]$. We will consider quench protocols where the Bloch vector $\vec{d}(k)$ characterizing the pre-quench Hamiltonian \hat{H} is changed to the vector $\vec{d}'(k)$ characterizing the post-quench Hamiltonian \hat{H}' . For such scenario, it can be seen that the Bloch vector $\vec{d}_P(k, t)$ is the solution of the differential equation [43, 44]:

$$\partial_t \vec{d}_P(k, t) = 2\vec{d}'(k) \times \vec{d}_P(k, t), \quad (2)$$

with initial condition $\vec{d}_P(k, 0) = \vec{d}(k)$. The solution to the above equation can be written as:

$$\begin{aligned} \vec{d}_P(k, t) = & \vec{d}_\parallel(k) + \cos[2d'(k)t] \vec{d}_\perp(k) + \\ & + \sin[2d'(k)t] \vec{d}_o(k), \end{aligned} \quad (3)$$

ESC	DQPT	DCN	exists (✓)/does not exist (✗)
yes	yes	yes	✓
no	yes	yes	✓
yes	no	yes	✗
no	no	yes	✗
yes	yes	no	✓
no	yes	no	✓
yes	no	no	✓
no	no	no	✓

TABLE I. Summary of our main results in the non-interacting case, showing the relations among ESCs, DQPTs, and DCN, for quenches in one-dimensional two-band models. The ✓ or ✗ for the rows mark the possibility or impossibility, respectively, of devising quench protocols featuring the corresponding combination of the three signatures in the subsequent unitary time-evolution.

where $d(k) \equiv |\vec{d}(k)|$ and $d'(k) \equiv |\vec{d}'(k)|$, and:

$$\vec{d}_\parallel(k) = \frac{[\vec{d}(k) \cdot \vec{d}'(k)]}{d'^2(k)} \vec{d}'(k), \quad (4a)$$

$$\vec{d}_\perp(k) = \vec{d}(k) - \vec{d}_\parallel(k), \quad (4b)$$

$$\vec{d}_o(k) = -\frac{\vec{d}(k) \times \vec{d}'(k)}{d'(k)}. \quad (4c)$$

The parent Hamiltonian offers a way of defining the notion of non-equilibrium topology in quantum quench problems. There are two *inequivalent* definitions of it. The approach followed by [43] and [44] is that of defining the non-equilibrium topology as the $(1+1)$ -dimensional topology of the of the parent Hamiltonian, i.e. taking time as an additional dimension. In Refs. [33, 34] instead, the topology of the time-evolved state is understood as the 1-dimensional topology of a band-flattened parent Hamiltonian, to which a classification similar to the equilibrium one is then applied. As we will emphasize in the following, for quenches within the same AZ class, looking at the DCN and the entanglement spectrum dynamics correspond to probing the two above definitions of non-equilibrium topology, respectively, while DQPTs occur for quenches crossing a quantum critical point [36, 37]. For general quantum quenches, not restricted to a given AZ class, we will show how these three signatures will become unrelated to any topology of the pre- or post-quench, or parent Hamiltonian. In the next section we review the definitions of entanglement spectrum, DQPTs and DCN, and how they can be calculated in non-interacting two-band systems.

1. Entanglement spectrum and its degeneracy

The entanglement spectrum for a quantum state $|\Psi\rangle$ of a given system is the set of the eigenvalues $\{\lambda_m\}$ of the reduced density matrix $\hat{\rho}_S = \text{Tr}_{\bar{S}} |\Psi\rangle\langle\Psi|$ for a subsystem

S of length $\ell < L$, where $\text{Tr}_{\bar{S}}$ denotes the partial trace over the complement \bar{S} of S in the total system. In the following, we will calculate the entanglement spectrum for the post-quench time-evolved state $|\Psi(t)\rangle$, choosing the subsystem S consisting of the first $\ell = L/2$ unit cells. The reduced density matrix $\hat{\rho}_S$ can be expressed as $\hat{\rho}_S = e^{-\hat{H}_S} / \text{Tr}[e^{-\hat{H}_S}]$, where the Hermitian operator \hat{H}_S is referred to as *entanglement Hamiltonian*. The ground-state of \hat{H}_S corresponds thus to the highest-weight eigenstate of $\hat{\rho}_S$. This notion offers a easy way of calculating the entanglement spectrum for non-interacting systems. There, \hat{H}_S can be shown to be a one-body operator of the form $\hat{H}_S = \sum_{i,j} h_{i,j}^S \hat{c}_i^\dagger \hat{c}_j$ (see e.g. Refs. [57, 58] and Appendix A 1), where in this section we denote with \hat{c}_j generic fermionic annihilation operator on site j , with j including possible orbital/spin degrees of freedom, and i, j belong to subsystem S . The single-particle spectrum $\{\epsilon_n\}$ of the entanglement Hamiltonian, i.e. the eigenvalues of the operator h^S in first quantization, can be calculated from knowledge of the single-particle density matrix C , with elements $C_{i,j} = \langle \Psi | \hat{c}_i^\dagger \hat{c}_j | \Psi \rangle$. Denoting with $\{\xi_n\}$ the spectrum of C , it can be shown that $\xi_n = (1 + e^{\epsilon_n})^{-1}$. Thus the eigenvalues λ_m of the entanglement spectrum are calculated by specifying the filling of the single-particle entanglement modes ϵ_n (see Refs. [57, 58] and Appendix A 1 for more details). For what follows, it is important to recall that there exists a connection between the topological nature of the state and the degeneracy of the eigenvalues in the entanglement spectrum [49–52]. In particular, for non-interacting systems, zero-energy modes in the spectrum of the parent Hamiltonian for $|\Psi\rangle$ with open boundary conditions imply the degeneracy of all the λ_m , as a consequence of zero-energy modes in the single-particle spectrum of the entanglement Hamiltonian appearing when the cut between the two subsystems S and \bar{S} is performed. A topological phase, generally endowed with zero-energy boundary modes by bulk-boundary correspondence, corresponds therefore to a degenerate entanglement spectrum (see Ref. [51] and Appendix A 1 for a discussion). The presence of ESCs specific times in the post-quench dynamics, hallmarks the presence of zero-energy modes in the spectrum of the parent Hamiltonian $\hat{H}_P(t)$, when open boundary conditions are considered. For quenches in the same AZ class, the dynamics of the entanglement spectrum corresponds to probing the 1-dimensional topology of the parent Hamiltonian at each instant in time [33, 34]: We will see however that for general quench protocols ESCs may appear as a consequence of boundary modes not related to a topological phase in the standard sense.

2. Dynamical phase transition

A DQPT is signaled by a non-analyticity of a rate function $f(t)$ at a certain instant of time t , where $f(t)$ is

defined as [35]:

$$f(t) = - \lim_{L \rightarrow +\infty} \frac{1}{L} \ln[\mathcal{L}(t)], \quad (5)$$

associated to the Loschmidt echo (a return probability) $\mathcal{L}(t) = |\langle \Psi | e^{-i\hat{H}'t} | \Psi \rangle|^2$, where $|\Psi\rangle$ denotes the initial state, commonly chosen to be the ground state of the pre-quench Hamiltonian. For two-band systems it is possible to show that (see Appendix A 2):

$$f(t) = - \int_{-\pi}^{\pi} \frac{dk}{2\pi} \ln [\cos^2[d'(k)t] + \gamma(k) \sin^2[d'(k)t]], \quad (6)$$

where $\gamma(k) = [\vec{n}'(k) \cdot \vec{n}(k)]^2$, $\vec{n}(k) = \vec{d}(k)/d(k)$ and $\vec{n}'(k) = \vec{d}'(k)/d'(k)$. From Eq. (6) we immediately observe that DQPTs occur when $\gamma(k^*) = 0$ for some momenta k^* . Furthermore, we notice that the expression for $\gamma(k)$ is independent of the direction of the quench, and so is the presence of DQPTs.

For quenches in the same AZ symmetry class, DQPTs were shown to be related to the change of topological properties of the Hamiltonians before and after the quench [36, 37]: In particular, in [37] a dynamical topological order parameter unambiguously capturing such change was introduced. In the following we will also provide example of DQPTs occurring after quenches between topologically trivial Hamiltonians.

3. Dynamical Chern number

The dynamical Chern number is defined for non-interacting models in one dimension, as the Chern number of the parent Hamiltonian in a $(1+1)$ -dimensional momentum-time domain. The DCN associated to a generic parent Hamiltonian $h_P(k, t) = \vec{d}_P(k, t) \cdot \vec{\sigma}$ is defined as [44]:

$$C_{\text{dyn}}^{(m)} = \int_{A_m} \frac{dk}{4\pi} \int_0^{T_k} dt \vec{n}_P(k, t) \cdot [\partial_k \vec{n}_P(k, t) \times \partial_t \vec{n}_P(k, t)], \quad (7)$$

measuring the number of times that $\vec{n}_P(k, t) = \vec{d}_P(k, t)/|\vec{d}_P(k, t)|$, with $\vec{d}_P(k, t)$ defined in Eq. (3), would cover the Bloch sphere in a reduced momentum-time manifold. This manifold is defined by the period of the time-evolution for the Bloch states with given momentum k , $T_k = \frac{\pi}{d'(k)}$, and the momentum interval $A_m \equiv [k_m, k_{m+1}]$, with $m = 1, \dots, N$, delimited by the two consecutive momenta k_m and k_{m+1} inside the first Brillouin zone $[-\pi, \pi)$ for which $\vec{n}(k_m) = \vec{d}(k_m)/|\vec{d}(k_m)|$ is parallel or anti-parallel to $\vec{n}'(k_m) = \vec{d}'(k_m)/|\vec{d}'(k_m)|$: For each of the k_m , $\vec{d}_P(k_m, t)$ is constant in time equal to its initial value $\vec{d}(k_m)$. If no such fixed momenta k_m are present, the domain of integration of Eq. (7)

is equivalent to a torus, since $\vec{d}_P(\pi, t) = \vec{d}_P(-\pi, t)$ and $\vec{d}_P(k, t + \pi/d'(k)) = \vec{d}_P(k, t)$. In the presence of N fixed momenta k_m , the domain of integration of Eq. (7) can be decomposed into N reduced momentum-time manifolds, each of them having the topology of a sphere, since the Bloch states at k_m do not evolve apart from a global phase. In this case, the DCN in Eq. (7) can be conveniently expressed as [44]:

$$C_{\text{dyn}}^{(m)} = \frac{1}{2} (\cos \theta_{k_m+1} - \cos \theta_{k_m}), \quad (8)$$

with θ_{k_m} being the angle between $\vec{n}(k_m)$ and $\vec{n}'(k_m)$. In the special case where the quench is performed within the same symmetry class of the Altland-Zirnbauer classification, the dynamical Chern number can be related to the winding numbers (BDI and AIII symmetry class) or to the \mathbb{Z}_2 topological numbers (D symmetry class) of the pre- and post-quench Hamiltonians. This suggests a relation between a finite DCN and the presence of DQPTs, which we will uncover later when presenting our results. For general quantum quenches, we will see how a finite DCN can arise quenching between two topologically trivial Hamiltonians, thus demonstrating how this indicator could be dynamically generated also in trivial cases.

III. NON-INTERACTING QUENCH DYNAMICS

This section is aimed at discussing the relations between DQPTs, DCNs and ESCs in non-interacting systems. First, we discuss the first four cases of Table I where the DCN is different from zero. We show that a finite DCN is a sufficient condition to have a DQPT, while there is no connection between the DCN and the presence of ESCs. Then, we address the four remaining cases of Table I characterized by a vanishing DCN and we study a simple quench protocol which allows us to show that there are no connections between ESCs and DQPTs either. Finally, we show that ESCs are accompanied by the appearance of zero-energy modes and discuss their topological origin. In the following, the vectors $\vec{d}(k)$ and $\vec{d}'(k)$ associated to the pre-quench and the post-quench Hamiltonians respectively fully determine the time-evolution of the system. As before, we set $\vec{n}(k) = \vec{d}(k)/|\vec{d}(k)|$ and $\vec{n}'(k) = \vec{d}'(k)/|\vec{d}'(k)|$.

A. Non-vanishing dynamical Chern number

1. Simultaneous presence of ESC and DQPT

We consider a system which is prepared in the ground state of a purely classical Hamiltonian and then evolves with the Su-Schrieffer-Heeger (SSH) Hamiltonian [56]. This corresponds to the case studied in Ref. [43]. We show in the following that the presence of ESCs probes

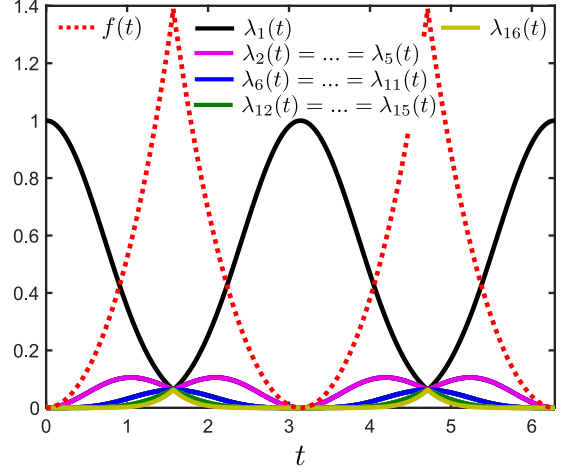


FIG. 1. Time evolution of the entanglement spectrum eigenvalues (solid lines) and of the rate function $f(t)$ (dashed red line) for the quench protocol: $\vec{d}(k) = (J_x, 0, 0)$ and $\vec{d}'(k) = (J_x \cos k, J_x \sin k, 0)$. Here $L = 1000$ sites and $J_x = 1$. In this case the ESCs and the DQPTs, signaled by the cusps in $f(t)$, appear at the same instants in time, while the DCN is finite (± 1).

in this case one-dimensional the topology of the parent Hamiltonian $H_P(t)$, and that their degeneracy is related to the number of edge modes in the spectrum of $H_P(t)$. The Bloch vectors $\vec{d}(k)$ and $\vec{d}'(k)$ corresponding to the pre-quench and the post-quench Hamiltonians are given by:

$$\vec{d}(k) = (J_x, 0, 0), \quad (9a)$$

$$\vec{d}'(k) = (J_x \cos k, J_x \sin k, 0), \quad (9b)$$

and are parallel and anti-parallel for $k = 0$ and $k = \pi$ respectively. This identifies two distinct momentum-time regions for the calculation of the DCN, and using Eq. (8) we observe that it is quantized to one (minus one) depending on which region we consider. The fact that the DCN for the total momentum-time zone sums to zero is a consequence of the particle-hole symmetry $C = \sigma_z \mathcal{K}$ of the model (with \mathcal{K} being the complex conjugation). The particle-hole is the only symmetry preserved in the time-evolution [33, 34], and at all times it relates the parent Bloch vectors $\vec{d}_P(k, t)$ and $\vec{d}_P(-k, t)$, implying that a positive covering of the Bloch sphere in one half of the momentum-time manifold must appear together with a negative one in the other half.

The Bloch vector $\vec{d}_P(k, t)$ of the parent Hamiltonian can be determined from Eq. (3) (see Appendix A3 for de-

tails):

$$d_P^{(x)}(k, t) = J_x - 2J_x \sin^2(J_x t) \sin^2 k, \quad (10a)$$

$$d_P^{(y)}(k, t) = J_x \sin^2(J_x t) \sin 2k, \quad (10b)$$

$$d_P^{(z)}(k, t) = -J_x \sin(2J_x t) \sin k, \quad (10c)$$

which is periodic in time with the same period π/J_x for each k . In Fig. 1 (solid lines) it can be seen that at times $t^* = \pi/(2J_x) + m\pi/J_x$ all the eigenvalues in the entanglement spectrum are degenerate. These ESCs are topological, in the sense that they stem from topologically protected boundary modes in the parent Hamiltonian appearing at times t^* , as we motivate in the following. From the above expression of the parent Hamiltonian it can be easily seen that at times $t^* = \pi/(2J_x) + m\pi/J_x$ it corresponds to a flat-band next-nearest-neighbor SSH model [59], i.e. $d_P(k, t^*) = (J_x \cos 2k, J_x \sin 2k, 0)$, with a restored chiral symmetry $S = \sigma_z$, such that $S h_P(k, t^*) S^\dagger = -h_P(k, t^*)$. The parent Hamiltonian $\hat{H}_P(t^*)$ with open boundary conditions therefore hosts four protected boundary modes at zero energy. This implies the presence of four zero-energy single-particle entanglement modes, when the half-system bipartition is considered. Since the parent Hamiltonian has flat bands, these four entanglement modes are the only ones contributing to the entanglement spectrum (see Appendix A 1). The number of non-zero eigenvalues in the entanglement spectrum is thus $2^4 = 16$, and the degeneracy of the four entanglement modes at $t = t^*$ forces all of them to be equal at these times, implying ESCs.

The presence of these ESCs is consistent with the out-of-equilibrium classification of Ref. [34]. The pre- and post-quench Hamiltonians (9a)-(9b) belong to class BDI, possessing time-reversal, particle-hole and chiral symmetry, and can be characterized by a \mathbb{Z} topological invariant (winding number). Since the only symmetry preserved in the time-evolution is the particle-hole [33, 34], the topology of the state out-of-equilibrium reduces to being classified by a \mathbb{Z}_2 invariant (e.g. the Zak phase, as we will define later on). This \mathbb{Z}_2 invariant, denoted with $\nu(t)$ in this section, can be calculated by looking at the real lattice momenta $k = 0, \pi$: We can compute it as $(-1)^{\nu(t)} = \text{sign}[d_P^{(x)}(0, t) d_P^{(x)}(\pi, t)]$, from which it can be seen that $\nu(t)$ equals 0, its starting value, at all times. Finally, the existence of DQPTs is inferred by calculating $\gamma(k) = [\vec{d}(k) \cdot \vec{d}'(k)]^2 = J_x^4 \cos^2 k$: For $k = \pi/2$ the system undergoes a DQPT at times $t^* = \pi/(2J_x) + m\pi/J_x$, as can be seen in Fig. 1 (dashed red line). The fact that in this example DQPTs and ESCs occur at the same times is a consequence of the post-quench Hamiltonian having flat bands. The presence of band dispersion makes the parent Hamiltonian not periodic in time anymore, and shifts the instants at which DQPTs occur away from the ESCs. This already hints to the fact that DQPTs and ESCs are unrelated.

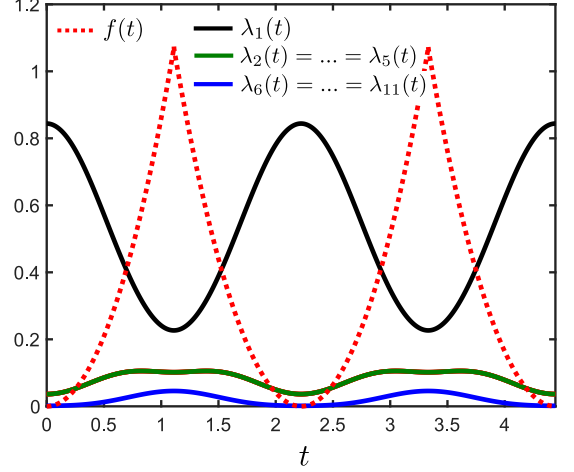


FIG. 2. Time evolution of the largest entanglement spectrum eigenvalues (solid lines) and of the rate function $f(t)$ (dashed red line) for the quench protocol: $\vec{d}(k) = (J_x, 0, J_z \cos k)$ and $\vec{d}'(k) = (J_x \cos k, J_x \sin k, J_z)$. Here $L = 1000$, $J_x = 1$ and $J_z = 1$. In this case, the presence of DQPTs is not accompanied by ESCs, while the DCN is finite (± 1).

2. Absence of ESCs and presence of DQPTs

In order to show that a finite DCN does not imply the presence of crossings in the entanglement spectrum, we consider a quantum quench determined by:

$$\vec{d}(k) = (J_x, 0, J_z \cos k), \quad (11a)$$

$$\vec{d}'(k) = (J_x \cos k, J_x \sin k, J_z). \quad (11b)$$

The vectors $\vec{n}(k)$ and $\vec{n}'(k)$ are parallel and anti-parallel for $k = 0$ and $k = \pi$, respectively, and using Eq. (8), it can be seen that the DCN is quantized to one, again indicating a full winding of the parent Bloch vector $\vec{n}_P(k, t)$ around the Bloch sphere in half of the momentum-time zone. We see that this DCN quantization does not correspond to any topological property of the pre- and post-quench Hamiltonian. Indeed the pre-quench Hamiltonian has a chiral symmetry but it cannot host any topological phase (the winding number is always zero), whereas the post-quench Hamiltonian corresponds to a flat-band Rice-Mele model [60] with a finite imbalance J_z which prevents the model to have any protecting symmetry. As we show in Fig. 2(a), there are no ESCs, while it is easy to see that DQPTs occurs when $t^* = (2m+1)\pi/\sqrt{J_x^2 + J_z^2}$ (see Fig. 2(b)).

It is worth to point out that a similar case (finite DCN and absence of ESCs) can happen also for quenches within the same AZ class. Considering for example class AIII, in Ref. [53] it was discussed how the ESCs became unstable under band dispersion of the post-quench Hamiltonian, despite quenching from a trivial to a topological phase, which implies a quantized DCN [44] (and

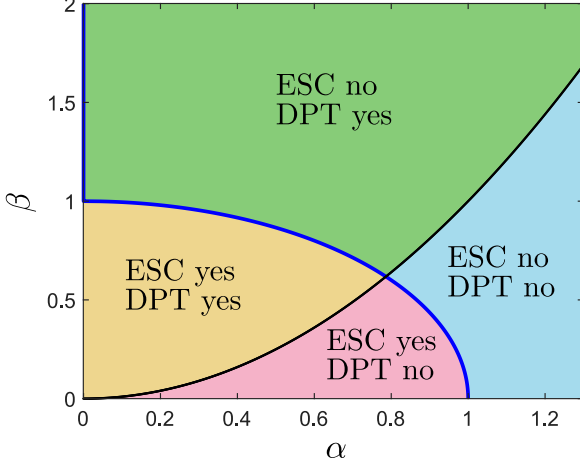


FIG. 3. For the quench protocol $\vec{d}(k) = J(\beta, 0, \alpha)$ to $\vec{d}'(k) = J(\cos k, \sin k, \alpha)$, the parameters α and β determine the existence of four regions where DQPTs and/or ESCs appear or do not appear. The existence of ESCs extends to the blue line as well (and thus for any $\alpha = 0$), which corresponds to the case of DCN quantized to one.

the presence of DQPTs, as we will see below). This exemplifies the fact that the (1+1)-dimensional topology of the parent Hamiltonian, measured by the DCN, in general does not reflect its 1-dimensional topology, which via bulk-boundary correspondence would become apparent as a degenerate entanglement spectrum.

3. Absence of DQPTs

This case cannot exist. In order to have a non-zero quantized DCN, we must have a fixed k^* inside the Brillouin zone such that $\vec{n}(k)$ and $\vec{n}'(k)$ are parallel, i.e. $\vec{n}(k^*) \cdot \vec{n}'(k^*) = 1$ and a fixed k^{**} such that $\vec{n}(k)$ and $\vec{n}'(k)$ are anti-parallel, i.e. $\vec{n}(k^{**}) \cdot \vec{n}'(k^{**}) = -1$. However, since the function $\vec{n}(k) \cdot \vec{n}'(k)$ must be continuous there must be a \bar{k} such that $\vec{n}(\bar{k}) \cdot \vec{n}'(\bar{k}) = \vec{d}(\bar{k}) \cdot \vec{d}'(\bar{k}) = 0$. This last equality implies the existence of a DQPT. For this reason, we observe that a quantized DCN is a sufficient (but not necessary) condition to have a DQPT.

B. Vanishing dynamical Chern number

The last four cases reported in Table I can be addressed by studying quantum quenches described by the following Bloch vectors:

$$\vec{d}(k) = (J_x, 0, J_z) \equiv J(\beta, 0, \alpha), \quad (12a)$$

$$\vec{d}'(k) = (J \cos k, J \sin k, J_z) \equiv J(\cos k, \sin k, \alpha), \quad (12b)$$

where we set $J_x = \beta J$ and $J_z = \alpha J$, with $\alpha > 0$ and $\beta > 0$ being dimensionless parameters. Since the vectors $\vec{n}(k)$ and $\vec{n}'(k)$ can never be anti-parallel, the DCN is vanishing for all α and β . This can be also checked by explicitly computing the DCN from Eq. (7), integrating over the whole momentum-time zone $[-\pi, \pi) \times [0, T)$ with $T = \frac{\pi}{J\sqrt{1+\alpha^2}}$: The result vanishes for any α and β , reflecting the fact that the parent Bloch vector $\vec{n}_P(k, t)$ does not wrap around the Bloch sphere. DQPTs occur (do not occur) when $|\alpha^2/\beta| < 1$ ($|\alpha^2/\beta| > 1$). As shown in Fig. 3, DQPTs and ESCs are completely independent. Indeed, by varying the parameters α and β , there exist four regions where any combination of the presence or absence of these features appears.

1. Entanglement spectrum crossings and zero-energy modes

For a proper choice of the parameters α and β the parent Hamiltonian for the quench protocol defined by Eqns. (12a)-(12b) exhibits ESCs, i.e. degeneracies of the entanglement spectrum at certain times. We now investigate in more details how such crossings are related to the presence of zero-energy modes. Preliminarily, we observe that for $\alpha = 0$ and $\beta = 1$ we recover the phenomenology studied in Subsection III A 1, with non-zero DCN. In particular, the emerging ESCs are associated to the zero-energy modes of a generalized SSH model with next-nearest-neighbor hopping terms supporting four zero-energy modes protected by a chiral symmetry. This result can be easily extended to the case $\beta \neq 1$.

We first notice that for $\alpha < 1$ and $\beta = 0$, the emerging ESCs are associated to the zero-energy modes of a SSH model with nearest-neighbor hopping terms (see Appendix A 3). In this case, the DCN is zero, however we obtain a non-trivial 1-dimensional topology of the parent Hamiltonian despite quenching between two topologically trivial models.

We now discuss the ESCs appearing for $\alpha \neq 0$ and $\beta \neq 0$ and we show that such crossings capture the presence of *accidental* zero-energy modes, i.e. zero-energy modes which are not associated to a standard symmetry protected topological phase. We proceed as follows. First we calculate the vector $\vec{d}_P(k, t)$ from Eq. (3) for the quantum quench defined in Eq. (12) (see Eq. (A15) in Appendix A 3 for a detailed expression). The corresponding parent Hamiltonian $h_P(k, t)$ can be written as:

$$h_P(k, t) = h_P^{(n.)}(k, t) + h_P^{(n.n.)}(k, t), \quad (13)$$

with:

$$h_P^{(n.n.)}(k, t) = \begin{pmatrix} 0 & \eta(t)e^{-2ik} \\ \eta^*(t)e^{2ik} & 0 \end{pmatrix}, \quad (14a)$$

$$h_P^{(n.)}(k, t) = \begin{pmatrix} M(k, t) & \delta(t) + \epsilon(t)e^{-ik} \\ \delta^*(t) + \epsilon^*(t)e^{ik} & -M(k, t) \end{pmatrix}, \quad (14b)$$

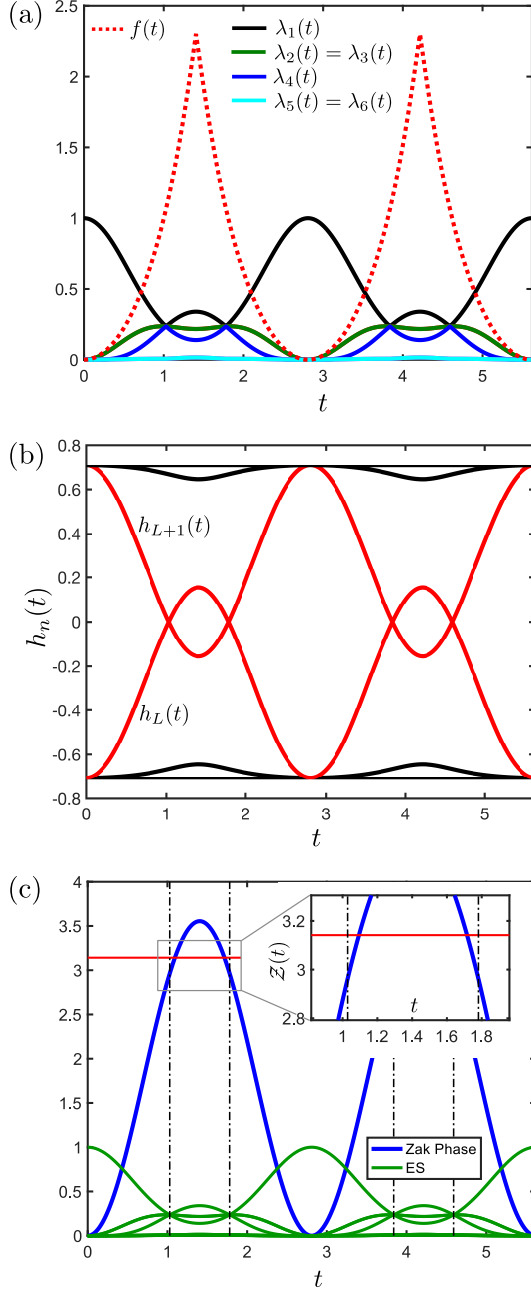


FIG. 4. Dynamics of various signatures for the quench protocol: $\vec{d}(k) = J(\beta, 0, \alpha)$ and $\vec{d}'(k) = J(\cos k, \sin k, \alpha)$ with $\alpha = \beta = 0.5$ and $J = 1$. (a) Time evolution of the entanglement spectrum $\lambda_m(t)$ (for $m = 1, \dots, 6$ — solid lines), and of the rate function $f(t)$ (dashed red line). (b) Time evolution of the eigenvalues $h_n(t)$ of the parent Hamiltonian $\hat{H}_P(t)$ with open boundary conditions. A pair of zero-energy modes appears when the entanglement spectrum is degenerate. (c) Time evolution of the Zak phase $\mathcal{Z}(t)$ of the parent Hamiltonian $h_P(k, t)$ (solid blue line). The Zak phase does not equal π (marked by the red horizontal line) at the times of the ESCs (marked by vertical dashed black lines — in green the entanglement spectrum for clarity), implying the absence of inversion as well as other possible protecting symmetries in the AZ sense.

with $M(k, t) = m(t) + m_c(t) \cos k + m_s(t) \sin k$. The explicit expressions of the functions $\delta(t)$, $\epsilon(t)$, $\eta(t)$, and $M(k, t)$ can be found in Appendix A 3. Given the parent Hamiltonian in momentum space we can easily obtain the parent Hamiltonian in real space, where we notice that $h_P^{(n)}(k, t)$ contains on-site terms plus nearest-neighbor hopping terms while $h_P^{(n,n)}(k, t)$ contains next-nearest-neighbor hopping contributions. By diagonalizing $\hat{H}_P(t)$ with open boundary conditions, we observe that zero-energy modes appear in its single-particle spectrum at the times when crossings in the entanglement spectrum happen. This is clear from Fig. 4(a) where we show the occurrence of ESCs accompanied by the appearance of (pairs of) zero-energy modes in the single-particle spectrum at the same times, shown in Fig. 4(b). A natural question which arises is whether these zero-energy modes are associated to a symmetry protected topological phase.

According to the Altland-Zirnbauer (AZ) classification of topological phases of matter, in one dimension, symmetry protected topological phases with zero-energy modes can appear in the presence of a chiral symmetry S such that $S h_P(k, t) S^\dagger = -h_P(k, t)$ (symmetry classes BDI and AIII) or in the presence of a particle-hole symmetry C such that $C h_P^*(k, t) C^\dagger = -h_P(-k, t)$ (symmetry class D). Since the matrix S must be k -independent, we observe that $S h_P(k, t) S^\dagger = -h_P(k, t)$ must hold for $h_P^{(n)}(k, t)$ and $h_P^{(n,n)}(k, t)$ separately, i.e.: $S h_P^{(n)}(k, t) S^\dagger = -h_P^{(n)}(k, t)$ and $S h_P^{(n,n)}(k, t) S^\dagger = -h_P^{(n,n)}(k, t)$. We can define a chiral symmetry $S = \sigma_z$ for the Hamiltonian $h^{(n,n)}(k, t)$, however one can immediately see that this is not a chiral symmetry for $h_P^{(n)}(k, t)$. Hence the zero-energy modes emerging during the time-evolution are not protected by an emergent chiral symmetry (this can be also seen by inspecting the winding of the parent Bloch vector shown in Fig. 10 in Appendix A 3). The presence of particle-hole and inversion symmetries is ruled out by analyzing the time-evolution of the Zak phase of $h_P(k, t)$, defined as [61, 62]:

$$\mathcal{Z}(t) = i \int_{-\pi}^{\pi} dk \langle u_P(k; t) | \partial_k u_P(k; t) \rangle, \quad (15)$$

with $|u_P(k; t)\rangle$ denoting the Bloch state of the lower band of $h_P(k, t)$. As shown in Fig. 4(c), the Zak phase is not quantized when the zero-energy modes appear. As long as $\alpha \neq 0$ and $\beta \neq 0$, these emerging zero-energy modes are thus determined by a fine tuning of the parameters in the parent Hamiltonian $h_P(k, t)$ and cannot be understood as standard zero-energy modes of a symmetry protected topological phase belonging to a fixed symmetry class of the AZ classification. One can intuitively understand this by first observing that the off-diagonal terms of $h_P(k, t)$ describe a generalized SSH model with nearest- and next-nearest-neighbor terms, and a chiral symmetry $S = \sigma_z$. Assuming for the moment the diagonal terms to be equal to zero, the generalized SSH

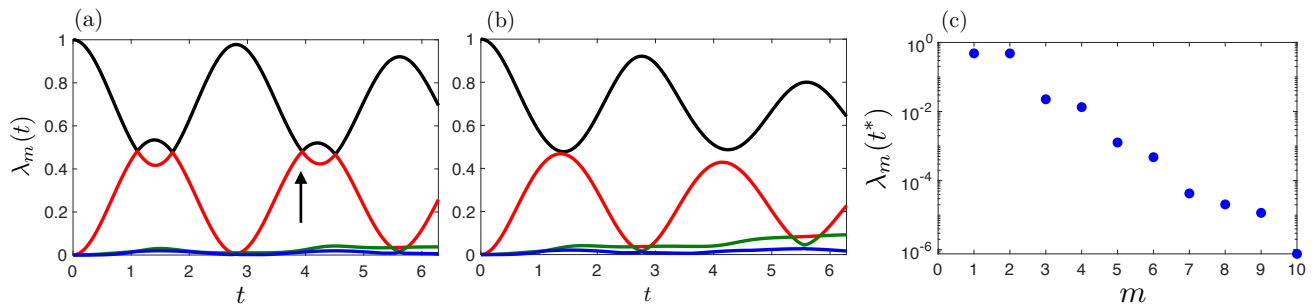


FIG. 5. Time-evolution of the four largest eigenvalues $\lambda_m(t)$ of the entanglement spectrum for the quench protocol: $\vec{d}(k) = J(\beta, 0, \alpha)$ and $\vec{d}'(k) = J(\cos k, \sin k, \alpha)$ with $\alpha = \beta = 0.5$ and different values of the Hubbard interaction term: $U = 0.5J$ (a), $U = J$ (b). (c) The entanglement spectrum at a fixed time t^* [see the black arrow in (a)] for which we have crossings between the two largest eigenvalues at $U = 0.5J$. Data obtained with DMRG for a chain of $L = 96$ unit cells with OBC and $J = 1$, using time step $dt = 0.0025$ (in units $1/J$). The truncation error is smaller than 10^{-12} at all times.

model can host four, two or zero exponentially localized zero-energy modes depending on the values of $\eta(t)$, $\epsilon(t)$, and $\delta(t)$. Let us now consider a fixed time t^* at which we have ESCs, e.g. $t^* \approx 1.028826$ in the case of $\alpha = \beta = 0.5$. In this case the off-diagonal terms alone, $\eta(t^*) = 1/3$, $\epsilon(t^*) = (1+i)/3$, and $\delta(t^*) = -i/6$, would determine the presence of two zero-energy modes protected by the chiral symmetry σ_z . The presence of diagonal terms breaks this chiral symmetry and generally would split these modes away from zero energy, still preserving their exponentially localized nature. However at time t^* the interplay of $m(t^*) = -1/6$, $m_c(t^*) = 1/3$, and $m_s(t^*) = -1/3$ constitutes a *fine-tuning* of diagonal elements which restores the two-fold degeneracy of the single-particle spectrum at zero energy, even though no chiral symmetry is present. These modes have therefore an underlying topological origin, coming from the generalized SSH model in absence of the diagonal terms, but their degeneracy at zero energy is a result of a particular choice of symmetry-breaking terms.

The presence of these *accidental* edge states at zero-energy in the spectrum of the flat-band parent Hamiltonian directly implies the presence of single-particle zero-energy modes in the spectrum of the entanglement Hamiltonian, thus yielding a degenerate entanglement spectrum at times $t^* + nT$ and $(T - t^*) + nT$ with $n \in \mathbb{N}$.

IV. INTERACTING QUENCH DYNAMICS

In this Section, by means of time-dependent DMRG, we study quench protocols in the presence of a Hubbard repulsive interaction $U \sum_j \hat{n}_{j,a} \hat{n}_{j,b}$, with $\hat{n}_{j,a} = \hat{a}_j^\dagger \hat{a}_j$ and $\hat{n}_{j,b} = \hat{b}_j^\dagger \hat{b}_j$ for one-dimensional two-band models. This Section is divided into two paragraphs. In the first one, we consider the quench protocol defined in Eq. (12) in the regime where α and β are tuned to have both DQPTs and ESCs in the non-interacting case and we show that the Hubbard interaction plays a detrimental role to their

presence, in the sense that DQPTs and ESCs disappear when U becomes sufficiently large. In the second paragraph, we investigate the opposite scenario, i.e. we show that DQPTs and ESCs can be generated by performing a quench of the interaction term. Our analysis is performed on an interacting SSH model in the flat band regime which can be addressed both numerically and analytically. The following numerical simulations have been performed using the ITensor library [<http://itensor.org>].

A. DQPTs and ESCs in the presence of interactions

We consider the quench protocol defined in Eq. (12) in the regime where $\alpha = \beta = 0.5$ such that, in the non interacting case, we have both DQPTs and ESCs. We switch on the repulsive Hubbard interaction U in the post-quench Hamiltonian, albeit we notice that this is equivalent to the case of having it switched on from the very beginning, being it $SU(2)$ invariant and since we start from a fully polarized state. In Fig. 5 we start investigating the time-evolution of the four largest eigenvalues $\lambda_m(t)$ of the entanglement spectrum for different values of the Hubbard interaction U (panels (a) and (b)). Preliminarily we observe that, because of the presence of interactions, the time-evolution is not periodic anymore and many eigenvalues of the entanglement spectrum become non-vanishing during the dynamics. In the presence of weak repulsive interactions, cf. Fig. 5(a), the entanglement spectrum crossings between the two largest eigenvalues are preserved, while they disappear for stronger interactions, cf. Fig. 5(b). In Fig. 5(c), we investigate the degeneracies of the entanglement spectrum at time $t = t^*$ for which we have a crossing between the two largest eigenvalues at $U = 0.5J$, cf. Fig. 5(a). Interestingly, we observe that only the two largest eigenvalues are degenerate, while the lowest ones are not. This is in stark contrast with the non-interacting case for which the entanglement spectrum is fully degenerate. We have

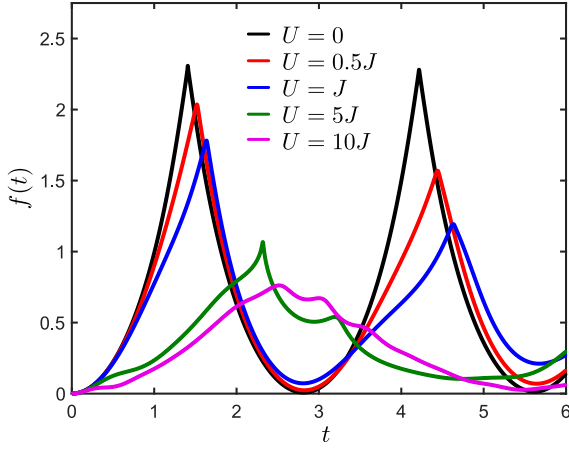


FIG. 6. The rate function $f(t)$ for the quantum quench $\vec{d}(k) = J(\beta, 0, \alpha)$ and $\vec{d}'(k) = J(\cos k, \sin k, \alpha)$ with $\alpha = \beta = 0.5$ for different values of the Hubbard interaction term U . Data obtained with DMRG for a chain of $L = 96$ unit cells with OBC and $J = 1$, using time step $dt = 0.001$. The truncation error is smaller than 10^{-12} at all times.

verified that this is not a finite size effect by increasing the size of the system up to $L = 244$ sites.

In Fig. 6 we show the behavior of the rate function $f(t)$ for different values of the interaction term. Similarly to the ESCs case, we observe that the divergences of the rate function $f(t)$ persist in the weakly interacting regime, while they disappear for larger interaction strengths, up to the timescales that we have investigated. We finally mention that the phenomenology observed here is qualitatively unaltered if we set $\alpha = 0$, namely considering the case of a quench of the form (9a)-(9b) in the SSH model.

B. Interacting SSH model

As a different scenario compared to what discussed before, here we consider interaction quenches in an interacting SSH model:

$$\hat{H} = \sum_j \left[\left(J \hat{a}_{j+1}^\dagger \hat{b}_j + J' \hat{a}_j^\dagger \hat{b}_j + \text{H.c.} \right) + U \hat{n}_{j,a} \hat{n}_{j,b} \right], \quad (16)$$

which supports at half-filling (the particle number N is equal to the number of sites L) a symmetry protected topological phase for $U < U_c$ and a trivial phase for $U > U_c$ with $U_c = 4J$ when $J' = 0$. The full phase diagram has been studied in Ref. [63]. In the following, for simplicity, we set $J' = 0$ and assume to prepare the system in a trivial state by choosing the pre-quench interaction $U > U_c$, and quench into the topological phase $U' < U_c$. We study this quantum quench protocol — that does not have a counterpart in the non-interacting regime in the sense that the single-particle hopping terms remain

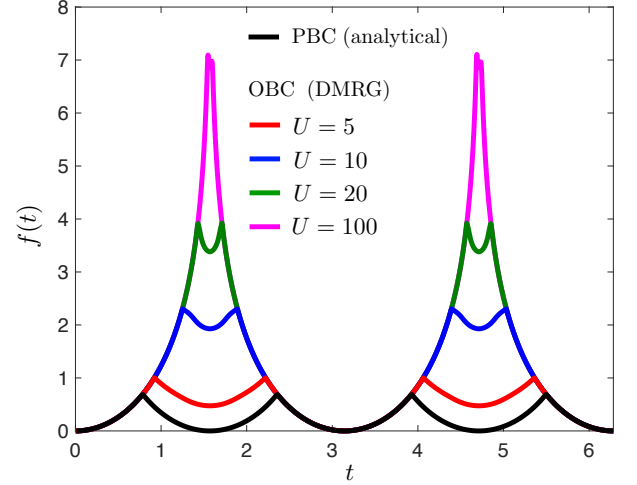


FIG. 7. Time evolution of the rate function $f(t)$ after a quench in the interacting SSH model from finite (large) U to $U' = 0$. Black line: $f(t)$ from Eq. (6), valid for PBC, for a quench from $U = 10J$ to $U' = 0$. Red, blue, green and violet lines show $f(t)$ from DMRG simulations with OBC, for a quenches to $U' = 0$ starting from $U = 5J, 10J, 20J$ and $100J$, respectively. In the plot $J = 1$, $L = 1056$, the time step $dt = 0.0025$ (in units $1/J$). The truncation error is smaller than 10^{-12} at all times.

constant — numerically assuming open boundary conditions (OBC) and analytically assuming periodic boundary conditions (PBC). We start our analysis assuming PBC and we discuss the existence of DQPTs. To this aim, we introduce the bond operators:

$$\begin{cases} \hat{w}_{j,+} = \frac{1}{\sqrt{2}} (\hat{a}_{j+1} + \hat{b}_j) \\ \hat{w}_{j,-} = \frac{1}{\sqrt{2}} (\hat{a}_{j+1} - \hat{b}_j) \end{cases}, \quad (17)$$

and define the $\mathfrak{su}(2)$ algebra operators:

$$\hat{T}_j^{(x)} = \hat{w}_{j,+}^\dagger \hat{w}_{j,-} + \hat{w}_{j,-}^\dagger \hat{w}_{j,+}, \quad (18a)$$

$$\hat{T}_j^{(y)} = -i(\hat{w}_{j,+}^\dagger \hat{w}_{j,-} - \hat{w}_{j,-}^\dagger \hat{w}_{j,+}), \quad (18b)$$

$$\hat{T}_j^{(z)} = \hat{w}_{j,+}^\dagger \hat{w}_{j,+} - \hat{w}_{j,-}^\dagger \hat{w}_{j,-}, \quad (18c)$$

satisfying the usual commutation relations $[\hat{T}_i^{(\alpha)}, \hat{T}_j^{(\beta)}] = 2i\epsilon_{\alpha\beta\gamma} \hat{T}_i^{(\gamma)} \delta_{ij}$. Then, we can map the Hamiltonian (16) onto an Ising chain in the presence of a transverse magnetic field [63]:

$$\hat{H} = \sum_j \left[J \hat{T}_j^{(z)} - \frac{U}{4} \hat{T}_{j-1}^{(x)} \hat{T}_j^{(x)} \right], \quad (19)$$

and observe that the paramagnetic (anti-ferromagnetic) phase of the Ising chain corresponds to the topological (trivial) phase of the interacting SSH model. Using a standard Jordan-Wigner transformation, the Hamiltonian (19) can be mapped onto a Kitaev chain. If

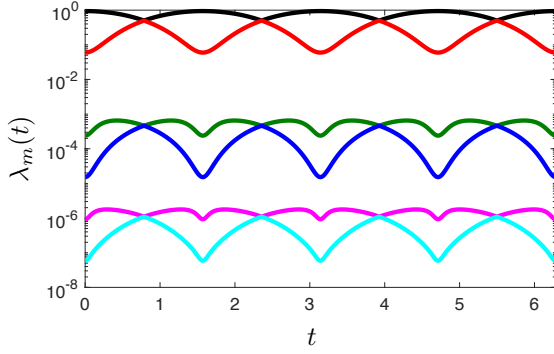


FIG. 8. Time-evolution of the six largest eigenvalues $\lambda_m(t)$ of the entanglement spectrum for a quench in the interacting SSH model from $U = 5J$ to $U' = 0$ with $J = 1$. Data obtained with DMRG on a chain of $L = 1056$ unit cells with OBC, with time step $dt = 0.0025$ (in units $1/J$). The truncation error is smaller than 10^{-12} at all times.

we define $\hat{c}_i = \hat{S}_{i-1} \hat{T}_i^-$ and $\hat{c}_i^\dagger = \hat{T}_i^+ \hat{S}_{i-1}$ with $\hat{T}_j^\pm = (\hat{T}_j^{(x)} \pm i\hat{T}_j^{(y)})/2$ and $\hat{S}_{i-1} = \prod_{j=1}^{i-1} e^{i\pi \hat{T}_j^+ \hat{T}_j^-}$ the usual string operator, we obtain:

$$\hat{H} = 2J \sum_i \hat{c}_i^\dagger \hat{c}_i - \frac{U}{4} \sum_i (\hat{c}_i^\dagger - \hat{c}_i)(\hat{c}_{i+1}^\dagger - \hat{c}_{i+1}). \quad (20)$$

Using the Nambu spinors $\hat{C}_k^\dagger = (\hat{c}_k^\dagger \ \hat{c}_{-k})$ in the momentum space representation, we can rewrite the Hamiltonian (20) as $\hat{H} = \sum_{k>0} \hat{C}_k^\dagger h(k) \hat{C}_k$, where $h(k) = \vec{d}(k) \cdot \vec{\sigma}$, with $\vec{d}(k) = (0, -U/2 \sin k, 2J - U/2 \cos k)$; similarly the vector $\vec{d}'(k)$ corresponding to the post-quench Hamiltonian is $\vec{d}'(k) = (0, -U'/2 \sin k, 2J - U'/2 \cos k)$. From now on, for simplicity, we set $J = 1$.

Before addressing the presence of DQPTs, we observe that, despite the presence of interactions, we are able to map the interacting SSH Hamiltonian (16) onto a quadratic Hamiltonian. Then, using Eq. (8), we can define a DCN for our quench protocol. In particular, the DCN is equal to one when the pre- and the post-quench Hamiltonian belong to two different phases and vanishes when they belong to the same phase. The existence of DQPTs with PBC can be then diagnosed using Eq. (6) applied to the Kitaev model obtained after the transformations (17) and (18). In the following we assume $U' = 0$ and observe that DPTs occur when $t^* = \pi/4 + n\pi/2$, see the red line data in Fig. (7), as long as $U > U_c$.

Using time-dependent DMRG with OBC we have studied the behavior of the rate function $f(t)$ defined in Eq. (5) by explicitly simulating the quench protocol for the Hamiltonian (16) for $U' = 0$ and different values of U . In Fig. 7 we compare our numerical DMRG data with the analytical prediction obtained using Eq. (6). We notice that the rate function $f(t)$ obtained from DMRG exhibits DQPTs, but not in correspondence of the times t^* obtained by means of Eq. (6) which is valid with PBC. This discrepancy is a direct consequence of the

open boundary conditions and it is not a finite-size effect. As explained in detail in Appendix B, the rate function $f(t)$ can be calculated analytically with OBC in the limit where $U' \rightarrow +\infty$, and is expected to exhibit DQPTs at $t^* = \pi/2 + n\pi$. This is in agreement with our DMRG simulations. For smaller values of U , DQPTs appear at different times. Finally, we study the time evolution of the eigenvalues of the entanglement spectrum. Since the mapping of the fermionic SSH model Eq. (16) in the case $J' = 0$ to a transverse-field Ising model (IV B) is non-local, as it makes use of the bond operators (17), the time evolution of the eigenvalues of the entanglement spectrum cannot be understood by exploiting this equivalence between the interacting SSH model and the Ising Hamiltonian. Therefore we explicitly simulate the time evolution of the interacting SSH model using DMRG and observe the appearance of entanglement spectrum crossings when quenching from the trivial to the topological phase. The results are shown in Fig. 8, for a quench from $U = 5J$ to $U' = 0$.

V. CONCLUDING DISCUSSION

In summary, we have investigated the relations between entanglement spectrum crossings (ESCs), dynamical quantum phase transitions (DQPTs) and quantized dynamical Chern number (DCN) in one-dimensional two-band models after a general quantum quench (i.e. not restricted to a given AZ class). In the case of non-interacting systems, we devised quench protocols after which basically any combination between ESCs, DQPTs and quantized DCN can occur (apart from the case of a quantized DCN without DQPTs — see Table I). While the absence of a one-to-one correspondence between these indicators had been previously discussed, here we showed that for general quenches also their relation to topology is in some cases lost. In particular, we were able to generate a finite DCN (see Sec. III A 2) or topological ESCs (see Sec. III B with $\beta = 0$ and $\alpha < 1$) from topologically trivial Hamiltonians, as well as *accidental* ESCs related to zero-energy boundary modes not protected by a conventional symmetry. Going beyond non-interacting systems, we also investigated the robustness of ESCs and DQPTs to the presence of repulsive Hubbard interactions: While DQPTs are found to persist up to moderate interaction strengths, the full degeneracy of the entanglement spectrum at the crossings does not strictly survive even at small interactions. Finally, we have considered interaction quenches in a SSH model showing, by means of DMRG simulations complemented by an analytical mapping onto a Ising chain in a transverse field, how ESCs and DQPTs can arise for such protocols.

We conclude by pointing out some possible future directions. An interesting point would be investigating the effects of finite temperature (see [64, 65] for a discussion in the context of DQPTs) in such quench problems: Can one identify indicators of some emergent topolog-

ical property, for example based on the observation of the entanglement spectrum, in the time-evolution after quenches with thermal states? Finally, our results raise the natural question of whether there is a more general way of understanding the appearance of the above signatures for quench protocols not constrained to a single AZ class. This question is of course relevant also beyond the realm of one-dimensional systems studied in this work.

ACKNOWLEDGMENTS

We acknowledge discussions with Jorge Cayao and Max McGinley. L.P. and J.C.B. acknowledge financial support from the DFG through SFB 1143 (Project No. 247310070). S.B. acknowledges the Hallwachs-Röntgen Postdoc Program of ct.qmat for financial support. Our numerical calculations were performed on resources at the TU Dresden Center for Information Services and High Performance Computing (ZIH).

Appendix A: Non-interacting quench dynamics

In this Appendix we review how the entanglement spectrum, and dynamical quantum phase transitions can be calculated in one-dimensional two-band models. We furthermore provide the explicit expression of the parent Hamiltonian for the quench protocol considered in section III B.

1. Entanglement spectrum and relation to topology

Here show how to calculate the entanglement spectrum for a non-interacting fermionic system [57, 58], and how topologically protected boundary modes imply a degeneracy if its levels. The physical properties of a non-interacting system can be calculated by using only the single-particle density matrix, which has elements $C_{i,j} = \langle \Psi | \hat{c}_i^\dagger \hat{c}_j | \Psi \rangle$, with $|\Psi\rangle$ being the state of the system, and \hat{c}_j being the fermionic operator which annihilate a fermion at site j (including possible spin/orbital degrees of freedom). In the following we discuss how to calculate the entanglement spectrum from the knowledge of the single-particle density matrix. The reduced density matrix $\hat{\rho}_S$ for a subsystem S of length $\ell < L$ can be written as:

$$\hat{\rho}_S = \frac{e^{-\hat{H}_S}}{Z_S} \quad \text{with} \quad Z_S = \text{Tr} \left[e^{-\hat{H}_S} \right], \quad (\text{A1})$$

where \hat{H}_S is referred to as the entanglement Hamiltonian. For non-interacting system all the correlations in S can be calculated from the single-particle density matrix using Wick's theorem: it follows that the entanglement Hamiltonian \hat{H}_S is quadratic in the fermionic operators,

i.e. $\hat{H}_S = \sum_{i,j=1}^{\ell} \hat{c}_i^\dagger h_{i,j}^S \hat{c}_j$. By introducing the operators \hat{d}_m which diagonalize \hat{H}_S , i.e. $\hat{H}_S = \sum_{m=1}^{\ell} \epsilon_m \hat{d}_m^\dagger \hat{d}_m$ with $\hat{c}_j = \sum_{m=1}^{\ell} V_{j,m} \hat{d}_m$, we can express $\hat{\rho}_S$ as:

$$\hat{\rho}_S = \prod_{m=1}^{\ell} \frac{e^{-\epsilon_m \hat{d}_m^\dagger \hat{d}_m}}{1 + e^{-\epsilon_m}}, \quad (\text{A2})$$

from which we can see that for j, k being lattice sites in subsystem S , we have:

$$\text{Tr}_S \left[\hat{\rho}_S \hat{c}_j^\dagger \hat{c}_k \right] = \sum_n \frac{V_{j,n}^* V_{k,n}}{1 + e^{\epsilon_n}}. \quad (\text{A3})$$

This gives us a direct relation between the eigenvalues ϵ_m of the entanglement Hamiltonian and the eigenvalues of the single-particle density matrix restricted to subsystem S . Namely, denoting with ξ_m the eigenvalues of the single-particle density matrix reduced to S , we have:

$$\xi_m = \frac{1}{1 + e^{\epsilon_m}}. \quad (\text{A4})$$

It is therefore sufficient to diagonalize the single-particle density matrix restricted to subsystem S for knowing the eigenvalues ϵ_m of the entanglement Hamiltonian \hat{H}_S , from which we can calculate the eigenvalues of the reduced density matrix $\hat{\rho}_S$ as:

$$\lambda_{\{s_m\}} = \prod_{m=1}^{\ell} \left[\frac{1}{2} + s_m \left(\xi_m - \frac{1}{2} \right) \right] \quad \text{with} \quad s_m = \pm 1. \quad (\text{A5})$$

In particular, the highest entanglement spectrum eigenvalue would correspond to occupying all the lowest eigenstates of \hat{H}_S with energy $\epsilon_m < 0$, i.e. $\xi_m > 1/2$, by setting $s_m = 1$ for them, and leaving the remaining ones empty with $s_m = -1$. The other eigenvalues are simply computed as excitations above this Fermi sea.

We point out now the relation between topology and the degeneracy of entanglement spectrum. First, we notice that there is a clear correspondence between the single-particle entanglement energies ϵ_m and the single-particle eigenvalues of the band-flattened parent Hamiltonian for the state $|\Psi\rangle$. Let us consider the band-flattened parent Hamiltonian defined as:

$$\hat{Q} = \hat{I} - 2 |\Psi\rangle \langle \Psi|. \quad (\text{A6})$$

It is immediate to notice that its single-particle representation Q , with elements $Q_{i,j} = \text{Tr} [\hat{Q} \hat{c}_i^\dagger \hat{c}_j]$ satisfies:

$$Q = I - 2C, \quad (\text{A7})$$

which gives a direct relation between its eigenvalues q_m and the entanglement energies ϵ_m , as:

$$q_m = 1 - 2\xi_m = \frac{e^{\epsilon_m} - 1}{e^{\epsilon_m} + 1}. \quad (\text{A8})$$

For $q_m = \pm 1$ (i.e. $\xi_m = 0, 1$) we have $\epsilon_m = \pm\infty$, thus the corresponding entanglement modes are *inert*, i.e. they are always empty/occupied and do not contribute to the entanglement spectrum. If Q has a zero-energy mode with $q_m = 0$, the entanglement Hamiltonian also has a single-particle energy mode with energy $\epsilon_m = 0$ (corresponding to $\xi_m = 1/2$). Now let us assume that $|\Psi\rangle$ is the ground state of a topological Hamiltonian $\hat{H} = \sum_{i,j=1}^L \hat{c}_i^\dagger H_{i,j} \hat{c}_j$ that admits protected zero-energy boundary modes with open boundary conditions. The entanglement spectrum would be computed by calculating C , which is equivalent to computing Q by flattening the bands of H . Since the band-flattening constitutes a smooth deformation which does not change the topological properties, Q is also expected to have protected zero-energy boundary modes, which in turn lead to zero modes in the entanglement energies, and thus degeneracies in the entanglement spectrum.

2. Dynamical quantum phase transitions

DQPTs are hallmarked by non-analyticities of the rate function:

$$f(t) = - \lim_{L \rightarrow +\infty} \frac{1}{L} \ln[\mathcal{L}(t)], \quad (\text{A9})$$

associated to the Loschmidt echo $\mathcal{L}(t) = |\langle \Psi | e^{-i\hat{H}'t} | \Psi \rangle|^2$, where $|\Psi\rangle$ is the initial quantum state. In this Appendix we briefly discuss under which conditions a DQPT can appear in two-band systems. To this end, we recall that the pre-quench Hamiltonian $\hat{H} = \sum_k \hat{\Pi}_k^\dagger h(k) \hat{\Pi}_k$, with $h(k) = \vec{d}(k) \cdot \vec{\sigma}$, can be diagonalized in momentum space by a unitary matrix M_k such that $M_k^\dagger h(k) M_k = E(k) \sigma_z$, yielding $\hat{H} = \sum_k E(k) \hat{\Phi}_k^\dagger \sigma_z \hat{\Phi}_k$ with $\hat{\Phi}_k^\dagger = \Pi_k^\dagger M_k = (\hat{c}_{k,U}^\dagger \ \hat{c}_{k,L}^\dagger)$. Similarly, the parent Hamiltonian $\hat{H} = \sum_k \hat{\Pi}_k^\dagger h_P(k, t) \hat{\Pi}_k$ is diagonalized at each time t by a matrix $M_k(t)$ such that $\hat{H}_P = \sum_k E(k) \hat{\Phi}_k^\dagger(t) \sigma_z \hat{\Phi}_k(t)$, with $\hat{\Phi}_k^\dagger(t) = \Pi_k^\dagger M_k(t) = (\hat{c}_{k,U}^\dagger(t) \ \hat{c}_{k,L}^\dagger(t))$. Taking the initial state $|\Psi\rangle$ as the ground-state of \hat{H} , we can express the initial and the time-evolved state as $|\Psi\rangle = \prod_k \hat{c}_{k,L}^\dagger |0\rangle = \prod_k \hat{\Pi}_k^\dagger U(k) |0\rangle$ and the time-evolved state $|\Psi(t)\rangle = \prod_k \hat{c}_{k,L}^\dagger(t) |0\rangle = \prod_k \hat{\Pi}_k^\dagger U(k, t) |0\rangle$, respectively, with the spinors U defined by $h(k)U(k) = -E(k)U(k)$

and $h_P(k, t)U(k, t) = -E(k)U(k, t)$. Using the definition (A9) we then obtain:

$$f(t) = - \int_{-\pi}^{+\pi} \frac{dk}{2\pi} \ln |U^\dagger(k)U(k, t)|^2, \quad (\text{A10})$$

where we used $\lim_{L \rightarrow +\infty} 1/L \sum_k \approx - \int_{-\pi}^{+\pi} dk / (2\pi)$. Defining $\vec{n}_P(k, t) = -\vec{d}_P(k, t)/d_P(k, t)$ and $\vec{n}(k) = -\vec{d}(k)/d(k)$ we see that:

$$\begin{aligned} |U(k)^\dagger U(k, t)|^2 &= \text{Tr} \left[\frac{1 + \vec{n}_P(k, t) \cdot \vec{\sigma}}{2} \frac{1 + \vec{n}(k) \cdot \vec{\sigma}}{2} \right] = \\ &= \frac{1}{2} [1 + \vec{n}_P(k, t) \cdot \vec{n}(k)], \end{aligned} \quad (\text{A11})$$

and using Eq. (4) we finally obtain:

$$f(t) = - \int_{-\pi}^{+\pi} \frac{dk}{2\pi} \ln [\cos^2[d'(k)t] + \gamma(k) \sin^2[d'(k)t]], \quad (\text{A12})$$

with $\gamma(k) = [\vec{n}'(k) \cdot \vec{n}(k)]^2$. Singularities of $f(t)$ come from those momenta k^* at which $\gamma(k^*) = 0$, happening periodically at times $t^* = (2n+1)\pi/d'(k^*)$, with $n \in \mathbb{N}$.

3. Parent Hamiltonian for two-band models

In this Appendix we calculate the explicit expressions (4a)-(4c) for the Hamiltonians:

$$\vec{d}(k) = (J_x, J_y, J_z), \quad (\text{A13a})$$

$$\vec{d}'(k) = (J' + J \cos k, J \sin k, \Delta). \quad (\text{A13b})$$

To this aim we conveniently introduce:

$$\begin{aligned} A(k) &\equiv \frac{[\vec{d}(k) \cdot \vec{d}'(k)]}{d'^2(k)} = \\ &= [(J' + J \cos k)J_x + JJ_y \sin k + J_z \Delta] / d'^2(k), \end{aligned} \quad (\text{A14})$$

with $d'(k) = \sqrt{(J' + J \cos k)^2 + J^2 \sin^2 k + \Delta^2}$ and using Eq. (3) we obtain:

$$d_P^{(x)}(k, t) = A(k)(J' + J \cos k) + \cos[2d'(k)t][J_x - A(k)(J' + J \cos k)] + \sin[2d'(k)t] \frac{JJ_z \sin k - \Delta J_y}{d'(k)}, \quad (\text{A15a})$$

$$d_P^{(y)}(k, t) = A(k)J \sin k + \cos[2d'(k)t][J_y - A(k) \sin k] + \sin[2d'(k)t] \frac{\Delta J_x - J_z(J' + J \cos k)}{d'(k)}, \quad (\text{A15b})$$

$$d_P^{(z)}(k, t) = A(k)\Delta + \cos[2d'(k)t][J_z - A(k)\Delta] + \sin[2d'(k)t] \frac{J_y(J' + J \cos k) - J_x J \sin k}{d'(k)}. \quad (\text{A15c})$$

In the case considered in the main text:

$$\vec{d}(k) = J(\beta, 0, \alpha), \quad (\text{A16a})$$

$$\vec{d}'(k) = J(\cos k, \sin k, \alpha), \quad (\text{A16b})$$

we obtain:

$$h_P(k, t) = \vec{d}_P(k, t) \cdot \vec{\sigma} = h_P^{(n.)}(k, t) + h_P^{(n.n.)}(k, t). \quad (\text{A17})$$

In the above equation:

$$h_P^{(n.n.)}(k, t) = \begin{pmatrix} 0 & \eta(t)e^{-2ik} \\ \eta(t)e^{2ik} & 0 \end{pmatrix}, \quad (\text{A18})$$

where:

$$\eta(t) = \frac{\beta J}{1 + \alpha^2} \sin^2(\sqrt{1 + \alpha^2} Jt), \quad (\text{A19})$$

and:

$$h_P^{(n.)}(k, t) = \begin{pmatrix} M(k, t) & \delta(t) + \epsilon(t)e^{-ik} \\ \delta^*(t) + \epsilon^*(t)e^{ik} & -M(k, t) \end{pmatrix} \quad (\text{A20})$$

with the off-diagonal terms being:

$$\epsilon(t) = \frac{\alpha J}{1 + \alpha^2} \left[\alpha \left(1 - \cos(2\sqrt{1 + \alpha^2} Jt) \right) + i\sqrt{1 + \alpha^2} \sin(2\sqrt{1 + \alpha^2} Jt) \right], \quad (\text{A21a})$$

$$\delta(t) = \frac{\beta J}{2(1 + \alpha^2)} \left[1 + (1 + 2\alpha^2) \cos(2\sqrt{1 + \alpha^2} Jt) + 2i\alpha\sqrt{1 + \alpha^2} \sin(2\sqrt{1 + \alpha^2} Jt) \right], \quad (\text{A21b})$$

and diagonal ones being:

$$M(k, t) = m(t) + m_s(t) \sin k + m_c(t) \cos k, \quad (\text{A21c})$$

$$m(t) = \frac{\alpha J}{1 + \alpha^2} \left[\alpha^2 + \cos(2\sqrt{1 + \alpha^2} Jt) \right], \quad (\text{A21d})$$

$$m_c(t) = \frac{2J\alpha\beta}{1 + \alpha^2} \sin^2(\sqrt{1 + \alpha^2} Jt), \quad (\text{A21e})$$

$$m_s(t) = -\frac{\beta}{\sqrt{1 + \alpha^2}} \sin(2\sqrt{1 + \alpha^2} Jt). \quad (\text{A21f})$$

a. Case of $\beta = 0$ and $\alpha < 1$

In the case of $\beta = 0$, the coefficients $\eta(t)$, $\delta(t)$, $m_c(t)$ and $m_s(t)$ vanish at all times, and the parent Hamiltonian becomes:

$$h_P(k, t) = \begin{pmatrix} m(t) & \epsilon(t)e^{-ik} \\ \epsilon^*(t)e^{ik} & -m(t) \end{pmatrix}. \quad (\text{A22})$$

For $\alpha < 1$, there exist time instants at which the diagonal term $m(t)$ vanishes, implying that at this times the parent Hamiltonian has a chiral symmetry $S = \sigma_z$ and a well

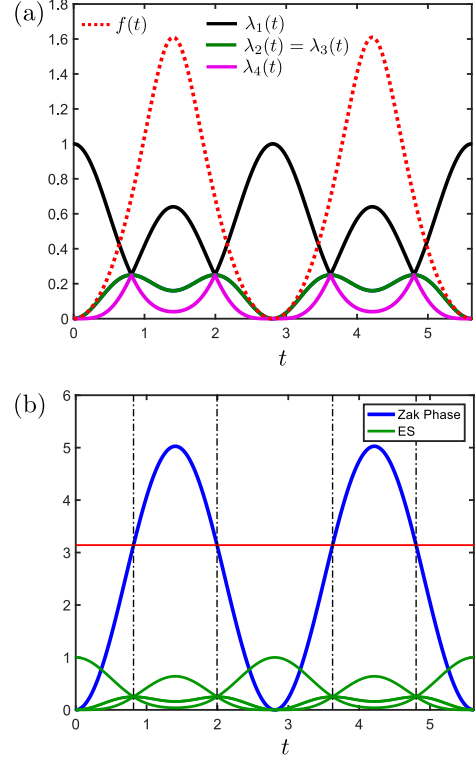


FIG. 9. Dynamics of various signatures for the quench protocol: $\vec{d}(k) = J(0, 0, \alpha)$ and $\vec{d}'(k) = J(\cos k, \sin k, \alpha)$ with $\alpha = 0.5$ and $J = 1$. (a) Time evolution of the entanglement spectrum $\lambda_m(t)$ (for $m = 1, \dots, 4$ — solid lines), and of the rate function $f(t)$ (dashed red line). (b) Time evolution of the Zak phase $Z(t)$ of the parent Hamiltonian $h_P(k, t)$ (solid blue line). The Zak phase equals π (marked by the red horizontal line) at the times of the ESCs (marked by vertical dashed black lines — in green the entanglement spectrum for clarity).

defined winding number 1. At these time instants crossings in the entanglement spectrum occur, as shown in Fig. 9(a), which are associated to the topologically protected edge states of the parent Hamiltonian when OBC are considered. This can be also seen by looking at the Zak phase, defined in Eq. (15), which is equal to π when the ESCs happen, as shown in Fig. 9(b).

b. Case of $\beta = \alpha = 0.5$

In the case of $J = 1$ and $\alpha = \beta = 0.5$, one can see that, at the time $t_1^* \approx 1.028826$ when the ESCs happen for the first time, the Bloch vector for the parent Hamiltonian takes the form:

$$\vec{d}_P(k, t_1^*) = \gamma \begin{pmatrix} 2(\cos k + \sin k) + 2 \cos 2k \\ 1 - 2(\cos k - \sin k) + 2 \sin 2k \\ 2(\cos k - \sin k) - 1 \end{pmatrix}, \quad (\text{A23})$$

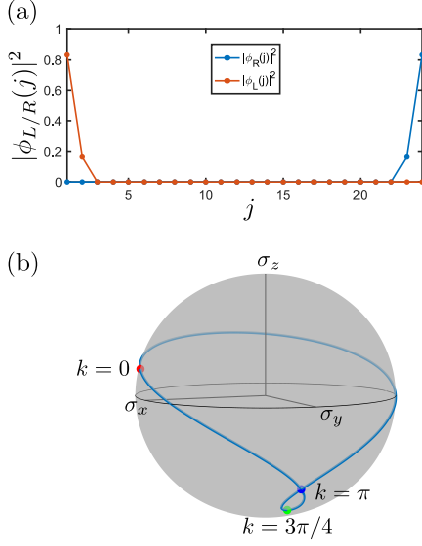


FIG. 10. (a) Density profile $|\phi_{L/R}(j)|^2 \equiv |\langle j, A | \phi_{L/R} \rangle|^2 + |\langle j, B | \phi_{L/R} \rangle|^2$ of the two zero-energy modes $|\phi_L\rangle$ and $|\phi_R\rangle$ of the parent Hamiltonian (A23) with OBC. (b) Evolution of $\vec{n}_P(k, t_1^*)$ as a function of k in the Brillouin zone.

with $\gamma = 1/6$, while at the second time t_2^* we have $\vec{d}_P(k, t_2^*) = \vec{d}_P(-k, t_1^*)$. The spectrum of these models with open boundary conditions have a pair of exponentially localized edge modes at zero energy, whose density profile is shown in Fig. 10(a), although no particle-hole, chiral or inversion symmetry is present, which can be seen from the fact that the Zak phase is different from π (see Fig. 4(c)), and also by looking at the evolution of $\vec{n}_P(k, t_1^*) = \vec{d}_P(k, t_1^*)/d_P(k, t_1^*)$ as a function of k in the Brillouin zone in Fig. 10(b).

Appendix B: Interacting quench dynamics

In this Appendix we report details regarding the calculation of dynamical phase transitions in the interacting models considered.

1. DQPT in interacting SSH model

Here we consider the quench protocol for the interacting SSH model presented in the Subsection IV B and we discuss how the choice of the boundary conditions affects the times t^* in correspondence of which DQPTs appear. We recall that the pre- and post-quench Hamiltonians are:

$$\hat{H} = \sum_{j=1}^{L_{BC}} \left(J \hat{a}_{j+1}^\dagger \hat{b}_j + \text{H.c.} \right) + U \sum_{j=1}^L \hat{n}_{j,a} \hat{n}_{j,b}, \quad (\text{B1})$$

and:

$$\hat{H}' = \sum_{j=1}^{L_{BC}} \left(J \hat{a}_{j+1}^\dagger \hat{b}_j + \text{H.c.} \right), \quad (\text{B2})$$

with $L_{BC} = L$ ($L_{BC} = L - 1$) for periodic (open) boundary conditions. In particular, we discuss the reason why, with open boundary conditions and in the regime $U \gg J$, DQPTs appear at $t^* = \pi/2 + n\pi/2$ (in units of J) rather than at $t^* = \pi/4 + n\pi/2$ as expected with periodic boundary conditions. In the regime $U \gg J$, using standard perturbation theory, it is easy to prove that the ground state of the pre-quench Hamiltonian is doubly degenerate, and the two lowest energy configurations are given by $|\Psi_A\rangle = \prod_{j=1}^L \hat{a}_j^\dagger |0\rangle$ and $|\Psi_B\rangle = \prod_{j=1}^L \hat{b}_j^\dagger |0\rangle$. Because of the inversion symmetry of the SSH Hamiltonian $\hat{I} = \sigma_x \otimes \hat{R}$ (with \hat{R} being the spatial reflection and σ_x acting on the sublattice indices), the two degenerate ground states correspond to the symmetric and the anti-symmetric linear combinations $|\Psi_\pm\rangle = (|\Psi_A\rangle \pm |\Psi_B\rangle)/\sqrt{2}$. Introducing the bond operators:

$$\begin{cases} \hat{w}_{j,+} = \frac{1}{\sqrt{2}} (\hat{a}_{j+1} + \hat{b}_j) \\ \hat{w}_{j,-} = \frac{1}{\sqrt{2}} (\hat{a}_{j+1} - \hat{b}_j) \end{cases}, \quad (\text{B3})$$

the post-quench Hamiltonian takes the form:

$$\hat{H}' = J \sum_{j=1}^{L-1} \left(\hat{w}_{j,+}^\dagger \hat{w}_{j,+} - \hat{w}_{j,-}^\dagger \hat{w}_{j,-} \right), \quad (\text{B4})$$

consisting of on-site terms only. For convenience we also define the single-particle states $|j, A\rangle = \hat{a}_j^\dagger |0\rangle$, $|j, B\rangle = \hat{b}_j^\dagger |0\rangle$ and $|j, +\rangle = \hat{w}_{j,+}^\dagger |0\rangle$ and $|j, -\rangle = \hat{w}_{j,-}^\dagger |0\rangle$. We observe that with open boundary conditions, $j = 1, \dots, L-1$ and the states $|1, A\rangle$ and $|L, B\rangle$ are completely decoupled. Since $|\Psi_A\rangle$ and $|\Psi_B\rangle$ are Slater determinants, under the action of the non-interacting post-quench Hamiltonian \hat{H}' , their single-particle states evolve in time as:

$$e^{-i\hat{H}'t} |j, A\rangle = e^{-it} |j-1, +\rangle - e^{it} |j-1, -\rangle, \quad (\text{B5a})$$

for $j = 1, \dots, L-1$ and:

$$e^{-i\hat{H}'t} |j, B\rangle = e^{-it} |j, +\rangle + e^{it} |j, -\rangle \quad (\text{B5b})$$

for $j = 2, \dots, L$. More explicitly we observe that, with open boundary conditions, the states $|1, A\rangle$ and $|L, B\rangle$ do not evolve. We now consider the time $t^* = \pi/2$ and, in order to diagnose the appearance of a DQPT, we calculate the overlap:

$$\begin{aligned} \langle \Psi_\pm | \Psi_\pm(t) \rangle &= \langle \Psi_A | \Psi_A(t) \rangle + \langle \Psi_B | \Psi_B(t) \rangle \pm \\ &+ (\langle \Psi_A | \Psi_B(t) \rangle + \langle \Psi_B | \Psi_A(t) \rangle). \end{aligned} \quad (\text{B6})$$

Using Eqs. (B5a)-(B5b), it is easy to prove that:

$$e^{-i\hat{H}'\frac{\pi}{2}} |j, A\rangle = -i |j-1, B\rangle, \quad (\text{B7a})$$

$$e^{-i\hat{H}'\frac{\pi}{2}} |j, B\rangle = -i |j+1, A\rangle. \quad (\text{B7b})$$

Using the fact that for two Slater determinants $|\Psi\rangle$ and $|\Phi\rangle$ made of L single-particle states $|\psi_j\rangle$ and $|\phi_j\rangle$ with $j = 1, \dots, L$, respectively, their overlap is given by the determinant of the single-particle overlap matrix, i.e. $\langle\Phi|\Psi\rangle = \det[\langle\phi_i|\psi_j\rangle]_{i,j}$, we observe that $\langle\Psi_A|\Psi_A(\pi/2)\rangle = \langle\Psi_B|\Psi_B(\pi/2)\rangle = 0$ with both OBC and PBC. We thus concentrate on $\langle\Psi_B|\Psi_A(\pi/2)\rangle$ (similar arguments hold for $\langle\Psi_A|\Psi_B(\pi/2)\rangle$). In the case of OBC since $|1, A\rangle$ remains unchanged, while all other $|j, A\rangle$ states in $|\Psi_A\rangle$ shift to B states, the overlap matrix has a column of zeros and therefore its determinant vanishes. Thus, at $t^* = \pi/2$ we have $\langle\Psi_\pm|\Psi_\pm(\pi/2)\rangle = 0$, which implies a DQPT. On the contrary, with PBC, it is possible to show that $\langle\Psi_\pm|\Psi_\pm(\pi/2)\rangle = \pm(-1)^{L/2}$, which implies that the rate function vanishes.

2. Calculation of rate function with DMRG

Here we discuss how to practically calculate the rate function $f(t)$ using matrix product states (MPS) techniques when the system size L becomes large. When the initial state $|\Psi\rangle$ and its time evolved $|\Psi(t)\rangle$ are expressed as MPS their overlap can be straightforwardly calculated. However, at times t^* at which we have a DPT we have that the rate function $f(t)$ defined in Eq. (5) becomes of order one, meaning that $|\langle\Psi|\Psi(t^*)\rangle|^2 \sim O(e^{-L})$. For large system sizes the value of $|\langle\Psi|\Psi(t^*)\rangle|^2$ is thus so small that it cannot be represented on a computer, thus yielding incorrect results. To overcome this problem, we iteratively rescale the overlap during its calculation in the MPS representation, to keep it of order one, and resum the logarithms of the rescaling factors at each step in order to access the rate function at the end of the calculation. Specifically, we calculate $\tilde{O}(t) = A(t)\langle\Psi|\Psi(t)\rangle$ with $A(t) = \prod_{j=1}^L \alpha_j(t)$, where the α_j are real rescaling

parameters chosen such that $|\tilde{O}(t)| \sim O(1)$, and in terms of $\tilde{O}(t)$ the rate function becomes:

$$f(t) = -\frac{1}{L} \log |\tilde{O}(t)|^2 + \frac{2}{L} \sum_{j=1}^L \log \alpha_j(t), \quad (\text{B8})$$

where the first term is now negligible if $|\tilde{O}(t)| \simeq 1$. We perform the following choice for the $\alpha_j(t)$. For MPS expressed as:

$$|\Psi\rangle = \sum_{\sigma_1, \dots, \sigma_L} M^{[1]\sigma_1} M^{[2]\sigma_2} \dots M^{[L]\sigma_L} |\sigma_1, \sigma_2, \dots, \sigma_L\rangle, \quad (\text{B9})$$

with σ_j denoting the occupation number at site j , and $M^{[j]\sigma_j}$ being matrices with elements $M_{a_{j-1}, a_j}^{[j]\sigma_j}$ (with $M^{[1]\sigma_1}$ and $M^{[L]\sigma_L}$ being row and column vectors respectively), and $|\Psi(t)\rangle$ having the same expression with different matrices \tilde{M} , the overlap is conveniently calculated by introducing matrices $C^{[j]}$ whose elements are given by:

$$C_{a_j, a'_j}^{[j]} = \sum_{\sigma_j} (M^{[j]\sigma_j})_{a_j, a_{j-1}}^\dagger C_{a_{j-1}, a'_{j-1}}^{[j-1]} \tilde{M}_{a'_{j-1}, a'_j}^{[j]\sigma_j}, \quad (\text{B10})$$

with $C^{[0]} = 1$ being the identity [55]. The overlap is then $\langle\Psi|\Psi(t)\rangle = C^{[L]}$. We compute the α_j by rescaling the $C^{[j]}$ at each step of the computation of the overlap $C^{[L]}$, that is for each j , $C^{[j]}$ is replaced by $\alpha_j C^{[j]}$ where:

$$\alpha_j = \text{tr}[(C^{[j]})^\dagger C^{[j]}]^{-\frac{1}{2}}, \quad (\text{B11})$$

which keep $|\tilde{O}(t)|$ of order one, therefore avoiding problems related to exponentially small numbers.

-
- [1] M. Z. Hasan and C. L. Kane, *Rev. Mod. Phys.* **82**, 3045 (2010).
 - [2] X.-L. Qi and S.-C. Zhang, *Rev. Mod. Phys.* **83**, 1057 (2011).
 - [3] X.-G. Wen, *Rev. Mod. Phys.* **89**, 041004 (2017).
 - [4] I. Bloch, J. Dalibard, W. Zwerger, *Rev. Mod. Phys.* **80**, 885 (2008).
 - [5] N. Goldman, G. Juzeliūnas, P. Öhberg, and I.B. Spielman, *Rep. Prog. Phys.* **77** 126401 (2014).
 - [6] M. Aidelsburger, S. Nascimbene, and N. Goldman, *C. R. Physique* **19** (2018) 394-432.
 - [7] N. Goldman, J. C. Budich, and P. Zoller, *Nat. Phys.* **12**, 639 (2016).
 - [8] A. Eckardt, *Rev. Mod. Phys.* **89**, 011004 (2017).
 - [9] N. R. Cooper, J. Dalibard, and I. B. Spielman *Rev. Mod. Phys.* **91**, 015005 (2019).
 - [10] M. S. Rudner and N. H. Lindner, *arXiv:1909.02008*.
 - [11] M. Aidelsburger, M. Atala, S. Nascimbene, S. Trotzky, Y.-A. Chen, and I. Bloch, *Phys. Rev. Lett.* **107**, 255301 (2011).
 - [12] J. Struck, C. Ölschläger, M. Weinberg, P. Hauke, J. Simonet, A. Eckardt, M. Lewenstein, K. Sengstock, and P. Windpassinger, *Phys. Rev. Lett.* **108**, 225304 (2012).
 - [13] J. Struck, M. Weinberg, C. Ölschläger, P. Windpassinger, J. Simonet, K. Sengstock, R. Häppner, P. Hauke, A. Eckardt, M. Lewenstein, and L. Mathey, *Nat. Phys.* **9**, 738 (2013).
 - [14] H. Miyake, G. A. Siviloglou, C. J. Kennedy, W. C. Burton, and W. Ketterle, *Phys. Rev. Lett.* **111**, 185302 (2013).
 - [15] M. Aidelsburger, M. Atala, M. Lohse, J. T. Barreiro, B. Paredes, and I. Bloch, *Phys. Rev. Lett.* **111**, 185301 (2013).
 - [16] G. Jotzu, M. Messer, R. Desbuquois, M. Lebrat, T. Uehlinger, D. Greif, and T. Esslinger, *Nature* **515**, 237 (2014).
 - [17] M. Mancini, G. Pagano, G. Cappellini, L. Livi, M. Rider, J. Catani, C. Sias, P. Zoller, M. Inguscio, M. Dalmonte, and L. Fallani, *Science* **349**, 1510 (2015).

- [18] B. K. Stuhl, H. I. Lu, L. M. Aycock, D. Genkina, and I. B. Spielman, *Science* **349**, 1514 (2015).
- [19] A. Bermudez, D. Patane, L. Amico, and M. A. Martin-Delgado, *Phys. Rev. Lett.* **102**, 135702 (2009).
- [20] M. S. Foster, M. Dzero, V. Gurarie, and E. A. Yuzbashyan, *Phys. Rev. B* **88**, 104511 (2013).
- [21] A. Rajak and A. Dutta, *Phys. Rev. E* **89**, 042125 (2014).
- [22] M. D. Caio, N. R. Cooper, and M. J. Bhaseen, *Phys. Rev. Lett.* **115**, 236403 (2015).
- [23] Y. Hu, P. Zoller, and J. C. Budich, *Phys. Rev. Lett.* **117**, 126803 (2016).
- [24] J. H. Wilson, J. C. W. Song, and G. Refael, *Phys. Rev. Lett.* **117**, 235302 (2016).
- [25] P. D. Sacramento, *Phys. Rev. E* **93**, 062117 (2016).
- [26] C. Wang, P. Zhang, X. Chen, J. Yu, and H. Zhai, *Phys. Rev. Lett.* **118**, 185701 (2017).
- [27] L. Barbiero, L. Santos, and N. Goldman, *Phys. Rev. B* **97**, 201115(R) (2018).
- [28] W. Sun, C.-R. Yi, B.-Z. Wang, W.-W. Zhang, B. C. Sanders, X.-T. Xu, Z.-Y. Wang, J. Schmiedmayer, Y. Deng, X.-J. Liu, S. Chen, and J.-W. Pan, *Phys. Rev. Lett.* **121**, 250403 (2018).
- [29] L. Zhang, L. Zhang, S. Niu, and X.-J. Liu, *Sci. Bull.* **63**, 1385 (2018).
- [30] T. V. Zache, N. Mueller, J. T. Schneider, F. Jendrzejewski, J. Berges, and P. Hauke, *Phys. Rev. Lett.* **122**, 050403 (2019).
- [31] S. Bandyopadhyay and A. Dutta, *Phys. Rev. B* **100**, 144302 (2019).
- [32] H. Hu and E. Zhao, [arXiv:1911.02211](https://arxiv.org/abs/1911.02211).
- [33] M. McGinley and N. R. Cooper, *Phys. Rev. Lett.* **121**, 090401 (2018).
- [34] M. McGinley and N. R. Cooper, *Phys. Rev. B* **99**, 075148 (2019).
- [35] M. Heyl, A. Polkovnikov, and S. Kehrein, *Phys. Rev. Lett.* **110**, 135704 (2013).
- [36] S. Vajna and B. Dóra, *Phys. Rev. B* **91**, 155127 (2015).
- [37] J. C. Budich and M. Heyl, *Phys. Rev. B* **93**, 085416 (2016).
- [38] N. Sedlmayr, P. Jaeger, M. Maiti, and J. Sirker, *Phys. Rev. B* **97**, 064304 (2016).
- [39] Z. Huang and A. V. Balatsky, *Phys. Rev. Lett.* **117**, 086802 (2016).
- [40] M. Heyl, *Rep. Prog. Phys.* **81**, 054001 (2018).
- [41] G. Torlai, L. Tagliacozzo, and G. De Chiara, *J. Stat. Mech.* P06001 (2014).
- [42] E. Canovi, E. Ercolessi, P. Naldesi, L. Taddia, and D. Vodola, *Phys. Rev. B* **89**, 104303 (2014).
- [43] Z. Gong and M. Ueda, *Phys. Rev. Lett.* **121**, 250601 (2018).
- [44] C. Yang, L. Li, and S. Chen, *Phys. Rev. B* **97**, 060304(R) (2018).
- [45] A. Altland, and M. R. Zirnbauer, *Phys. Rev. B* **55**, 1142 (1997).
- [46] A. P. Schnyder, S. Ryu, A. Furusaki, and A. W. W. Ludwig, *Phys. Rev. B* **78**, 195125 (2008).
- [47] A. W. W. Ludwig, *Phys. Scr.* **T168**, 014001 (2016).
- [48] C. B. Mendl, J. C. Budich, *Phys. Rev. B* **100**, 224307 (2019).
- [49] L. Fidkowski, *Phys. Rev. Lett.* **104**, 130502 (2010).
- [50] F. Pollmann, A. M. Turner, E. Berg, and M. Oshikawa, *Phys. Rev. B* **81**, 064439 (2010).
- [51] A. M. Turner, Y. Zhang, and A. Vishwanath, *Phys. Rev. B* **82**, 241102(R) (2010).
- [52] A. M. Turner, F. Pollmann, and E. Berg, *Phys. Rev. B* **83**, 075102 (2011).
- [53] S. Lu and J. Yu, *Phys. Rev. A* **99**, 033621 (2019).
- [54] S. R. White, *Phys. Rev. Lett.* **69**, 2863 (1992).
- [55] U. Schollwöck, *Ann. Phys.* **326**, 96 (2011).
- [56] W.-P. Su, J. R. Schrieffer, and A. J. Heeger, *Phys. Rev. Lett.* **42**, 1698 (1979).
- [57] G. Vidal, J. I. Latorre, E. Rico, and A. Kitaev, *Phys. Rev. Lett.* **90**, 227902 (2003).
- [58] I. Peschel and V. Eisler, *J. Phys. A: Math. Theor.* **42**, 504003 (2009).
- [59] L. Li, Z. Xu, and S. Chen *Phys. Rev. B* **89**, 085111 (2014).
- [60] M. J. Rice and E. J. Mele *Phys. Rev. Lett.* **49**, 1455 (1982).
- [61] J. Zak, *Phys. Rev. Lett.* **62**, 2747 (1989).
- [62] R. Resta, *J. Phys.: Condens. Matter* **12** R107 (2000).
- [63] J. Jünemann, A. Piga, S.-J. Ran, M. Lewenstein, M. Rizzi, and A. Bermudez, *Phys. Rev. X* **7**, 031057 (2017).
- [64] U. Bhattacharya, S. Bandyopadhyay, and A. Dutta, *Phys. Rev. B* **96**, 180303(R) (2017).
- [65] M. Heyl and J. C. Budich, *Phys. Rev. B* **96**, 180304(R) (2017).